Surface Characteristics of the Micro-pore and Nanotube Formed Ti-25Nb-7Hf Alloy for Biomaterials

朝 鮮 大 學 校　大 學 院

光技術工學科(光應用工學專攻)

金　　晟　　煥

Surface Characteristics of the Micro-pore and Nanotube Formed Ti-25Nb-7Hf Alloy for Biomaterials

마이크로 포아와 나노튜브 형성 된 생체용 Ti-25Nb-7Hf 합금의 표면특성

2014年 2月 25日

朝鮮大學校 大學院

光技術工學科(光應用工學專攻)

金 晟 煥

Surface Characteristics of the Micro-pore and Nanotube Formed Ti-25Nb-7Hf Alloy for Biomaterials

指導教授   崔 漢 喆

이 論文을 工學 碩士學位申請 論文으로 提出함

2013年 10月

朝鮮大學校 大學院

光技術工學科(光應用工學專攻)

金 晟 煥

金晟煥의 碩士學位論文을 認准함

委 員 長　朝鮮大學校　　　敎　授　　孫 美 敬　印

委　　員　朝鮮大學校　　　敎　授　柳　　薰　印

委　　員　朝鮮大學校　　　敎　授　崔 漢 喆　印

2013年　11月

朝 鮮 大 學 校　大 學 院

CONTENTS

LIST OF TABLES

LIST OF FIGURES

국 문 초 록

마이크로 포아와 나노튜브 형성 된 생체용 Ti-25Nb-7Hf 합금의 표면특성

김 성 환

지도교수: 최한철, 공학/치의학박사

광기술공학과(광응용공학전공)

조선대학교 대학원

본 논문에서는, 두 단계 양극산화법을 이용하여 표면에 마이크로 포아와 나노튜브를 형성 하여 합금표면에 마이크로와 나노구조의 거칠기를 부여함으로써 뼈와의 골 융합성을 극대화시키는 연구를 진행하였다. Ti-25Nb-7Hf 삼원계 합금은 Ti-25Nb 이원계 합금을 기본으로 하여 Hf 함량을 7 wt.% 가 되도록 아크용해법을 이용하여 합금을 설계하였다. 제조된 합금은 균질화 처리를 위해 1000 ℃에서 12시간동안 열처리한 후 급냉하여 준비하였다. 표면에 두 가지 구조를 형성하기 위해 먼저 200 V 전위에서 3분 동안 1 M H_3PO_4의 용액에서 마이크로 포아를 형성 후 1 M H_3PO_4용액에 소량의 NaF를 첨가한 전해질 용액에서 30 V, 2시간 동안 나노튜브를 형성하였다, 모든 시험편의 표면은 OM, FE-SEM, EDS, XRD, 및 STEM 등으로 분석하였다. 표면의 전기화학적 부식 거동은 동전위 분극시험으로 분석하였고, 두 단계로 마이크로 포아 형성 후 나노튜브를 형성 한 Ti-25Nb-xHf 합금 표면의 접촉각을 측정하여 표면 젖음성을 평가하여 다음과 같은 결과를 얻었다.

1. X 선 회절 분석 결과, Ti-25Nb 이원계 합금에서는 α″ 상으로 구성되었고, Ti-25Nb-7Hf 합금의 미세조직은 α″ + β 상이 관찰되었다. 또한, Hf함량이 첨가됨으로써 마르텐사이트 α″ 구조에서 α″ + β 상을 갖는 등축정 구조를 나타내었다.
2. 마이크로 포아 형성 후 표면 관찰 결과 Hf가 첨가됨에 따라 포아수가 감소하고

포아 크기가 증가하였으며 anatase와 rutile상의 산화막이 형성되었다.

3. 나노튜브의 형성은 Hf함량이 첨가되면 튜브의 길이가 증가하고, 튜브의 배열이 불규칙에서 규칙적으로 변화되었다. 인가전위가 증가할수록 나노튜브의 직경이 증가되었으며, 나노튜브형성 시간이 증가할수록 튜브 길이가 증가하였다.

4. 마이크로 포아 형성 후 나노튜브를 형성 한 경우 마이크로 포아 속에 나노튜브가 형성되었다.

5. 양극 분극 곡선으로부터, 두 단계로 마이크로 포아 형성 후 나노튜브 형성한 Ti-25Nb-7Hf 합금은 아무처리 하지 않은 합금과 마이크로 포아만 형성한 합금보다 낮은 부식전위와 높은 부식전류밀도를 보였다.

6. 접촉각 측정으로부터, 두 단계로 마이크로 포아 형성 후 나노튜브 형성 한 표면이 가장 우수한 젖음성을 나타내었다.

결론적으로, 두 단계로 마이크로 포아 형성 후 나노튜브를 형성한 Ti-25Nb-7Hf 합금은 마이크로와 나노 구조를 형성하여 넓은 비표면적을 제공함으로서 생체적합성이 우수한 표면처리로 응용될 수 있을 것으로 생각된다.

Ⅰ. INTRODUCTION

Titanium (Ti) and its alloys have been studied an implant material from 1940s. Because, it show many advantages, such as good biocompatibility, corrosion resistance, low elastic modulus and mechanical properties to have an application for biomaterials fields [1]. Ti-6Al-4V alloy is widely used for implant parts. However, there are some problems of the alloy such as toxicity of V element and Alzheimer's disease of Al element [2]. According to the studies on cytotoxicity of pure metals, Ti alloys consisting of niobium (Nb), zirconium (Zr), tantalum (Ta), and hafnium (Hf) elements would be recommended. So, some researchers have focused on Ti-Nb-Zr, Ti-Ta-Zr, Ti-Nb-Hf, and Ti-Ta-Hf alloy system with controlling the contents as recommended elements [3-5]. Especially, Nb is one of the most effective Ti β-stabilizers and the atoms occupy the Ti sites resulting in solid-solution strengthening. Also, Ti alloyed with Hf will likely to have good corrosion resistance and Hf shows complete mutual solubility in both α and β structured Ti phases [6]. Therefore, the superior properties of Nb and Hf are the forces driving the introduction of Ti-Nb-Hf alloy into biomaterials.

Various surface modifications on Ti implants have been carried out to improve their bioactivity. The phenomena of anodization occurs at the moment of dielectric breakdown, Ti ions in the Ti alloy and OH ions in the electrolyte move in opposite directions very quickly to from TiO_2 again, this process is referred to as micro-arc oxidation or anodic spark oxidation. The micro-arc oxidation has been increased attractive attentions to improve a surface property, that is the adhesion to substrate metal, including corrosion, and biocompatibility of alloy surfaces [7-9]. The applications of micro-arc oxidation to the surface characteristics of Ti alloys has been proposed in order to improve their adhesive properties when used with organic adhesives and improvement of their biocompatibility [10]. From previous report, anodized TiO_2 surface provided higher cell adhesion,

proliferation, and cells cultured on anodized TiO_2 surfaces demonstrated higher ALP activity, compared with the Ti control surface [11].

Titanium oxide (TiO_2) nanotubes are of considerable interests for their applications due to their unique physical and chemical properties. Self-organized TiO_2 nanotube has been produced in fluoride-containing electrolytes, chromic acid-HF mixtures and H_3PO_4-NaF mixtures [12]. It is reported in the literature that nanotubes of morphologies on Ti alloys can be achieved by changing the applied potential, time, and alloying elements [13, 14]. From previously reported research, as the anodizing potential increased, the diameter and thickness of the nanotube increased. As the anodization time increased, the nanotube thickness increased [4, 15, 16]. Also, nanotubes have been used to improve bone tissue integration and the size is important in cell adhesion [17, 18].

Related information on the surface morphology and characteristics of the micro-pore and nanotube formed Ti-Nb-Hf alloy by two step anodization method is very limited. Therefore, the purpose of the present study was to investigate the surface characteristics of the micro-pore and nanotube formed Ti-25Nb-7Hf alloy for biomaterials.

Ⅱ. BACKGROUND

2.1. Titanium [19]

Ti is widely distributed in the universe. It is abundant on earth and has been detected in meteorites and other stars. Its concentration within the earth's crust of about 0.6% makes it the fourth most abundant of the metals after aluminium (Al), iron (Fe) and magnesium (Mg). There are 20 times more in quantity than chromium (Cr), 30 times more than nickel (Ni), 60 times more than copper (Cu), 600 times more than molybdenum (Mo). Some of the physical properties of Ti are listed in Table 1.

Table 1. Physical properties of Ti [20]

Name of element	Atomic symbol	Atomic number	Atomic weight	Density (g/cm^3)	Boiling point (°C)	Melting point (°C)
Titanium	Ti	22	47.90	4.5	3130	1812

2.1.1 Classification of Ti alloy [19]

Ti exists in two crystallographic forms. At room temperature, commercially pure titanium (CP-Ti) has a hexagonal close-packed (hcp) crystal structure referred to as α-phase. At 883 ℃, this transforms to a body-centered cubic (bcc) structure known as β-phase. The manipulation of these crystallographic variations through alloying additions and thermochemical processing is the basis for the development of a wide range of alloys and properties. The alloying elements have different influences on the properties of Ti. Some of the most common alloying elements and their stabilizing effect are shown in Table 2. On the other hand, elements such as nitrogen, carbon and especially oxygen have a strong α-stabilizing effect and thereby raise the α→β transition temperature (β-transus), whereas hydrogen, which has a β-stabilizing effect, lowers the transus temperature. Increasing the amount of interstitial elements leads to a drastic increase in strength (Fig. 1), but at the same time, leads to a sharp drop in ductility and with an increased risk of embrittlement. Based on the phases present, Ti alloys can be classified as α alloys, β alloys or α+β alloys. Within the last category are the subclasses near-α and near-β, referring to alloys with compositions which place them near to α/(α+β) or (α+β)/β-phase boundaries, respectively. The α alloys contain elements such as Al. These α-stabilizing elements increase the phase transformation temperature. They are characterized by satisfactory strength, toughness and weldability but poorer forgeability than β alloys. The absence of a ductile - brittle transformation, a property of the bcc structure, makes a alloys suitable for cryogenic applications. α+β alloys have a composition that supports a mixture of α and β phases. α+β alloys generally exhibit good fabricability as well as high room temperature strength and moderate elevated-temperature strength. The most commonly used α+β alloy is Ti-6Al-4V. The β alloys contain elements such as V, Mo, Fe and Cr, which

decrease the temperature of the α to β phase transition. β alloys are extremely formable. They are also prone to ductile-brittle transformation, and along with other bcc-phase alloys, are unsuitable for low-temperature application. The most commonly used titanium alloys are presented in phase-diagram format, Fig. 2, to show the interactions between the alloys's α- and β -stabilizing components.

Table 2. Common alloying elements and their stabilizing effect [21]

Alloying element	Range (wt.%)	Effect on structure
Aluminium	2 to 7	α-stabilizer
Tin	2 to 6	α-stabilizer
Vanadium	2 to 20	β-stabilizer
Molybdenum	2 to 20	β-stabilizer
Chromium	2 to 12	β-stabilizer
Copper	2 to 6	β-stabilizer
Zirconium	2 to 8	α and β strengthening
Silicon	0.2 to 1	Improves creep resistance
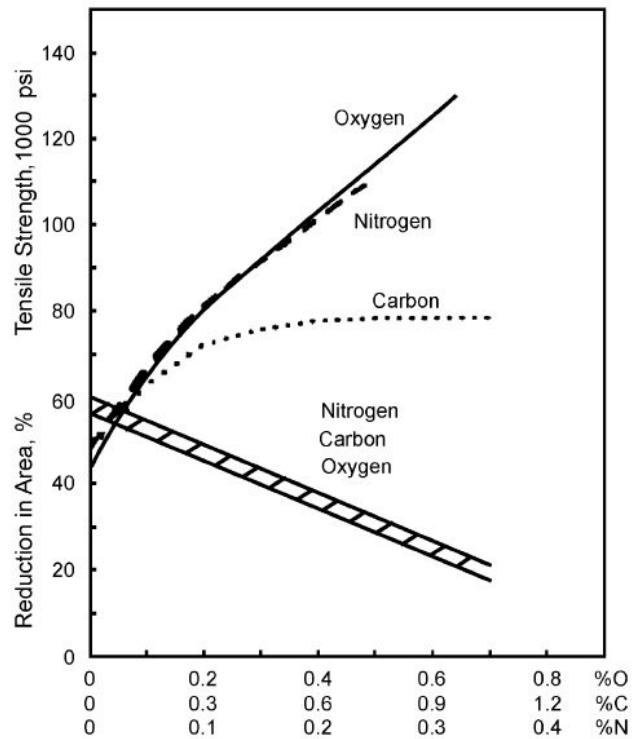
Fig. 1. Effect of interstitial alloying elements on strength and reduction
    in area of Ti [22].
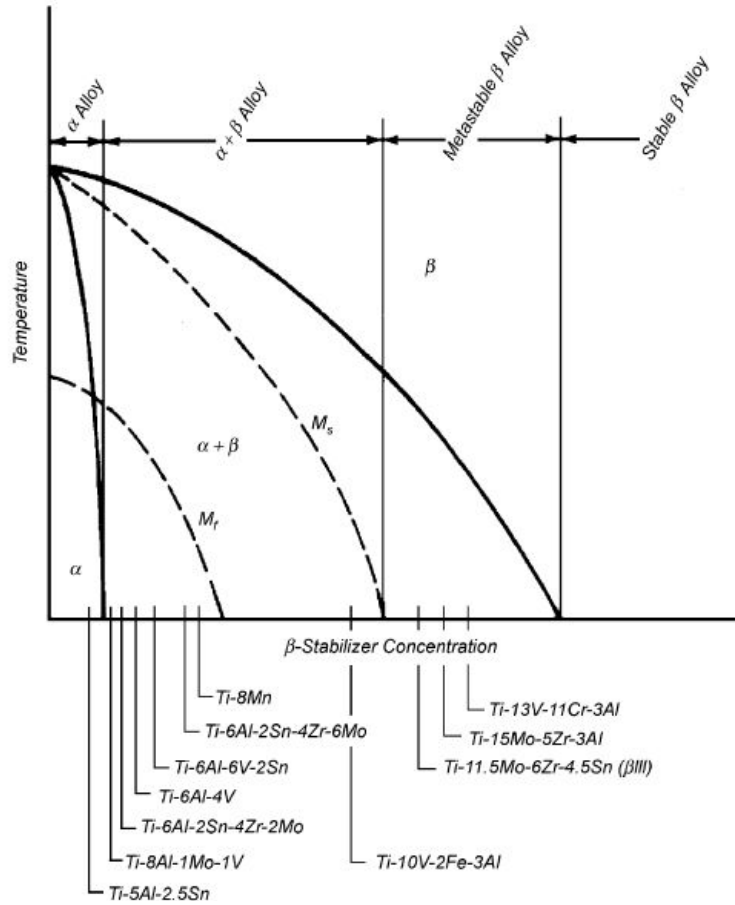
Fig. 2. Compositions of U. S. technical alloys mapped onto a pseudobinary β
    -isomorphous phase diagram [23].

2.1.2. Ti-Nb-Hf system

About the alloying element of Ti alloys for dental application, many studies have focused on the development of Al and V fee Ti alloys. So, current research on metallic biomaterials has focused on Ti alloys composed of non-toxic elements like Ta, Hf, Nb and Zr [24]. The Ti-Nb alloy has demonstrated a great potential for implant material. For example, the Ti-25Nb had a bending strength of 1650 MPa and bending moulus of 77 GPa [25]. Also, the Ti-Nb alloys have presented superior corrosion resistance when compared with the Ti-6Al-4V alloy. Assis [26] has reported a slightly improved corrosion resistance associated to the Ti-13Nb-13Zr compared with the Ti-6Al-4V alloy. Hf shows complete mutual solubilities in both α and β structured Ti phases, the same as Zr elements. Also Ti alloyed with Hf will likely to have good corrosion resistance [16]. From previously reported research [27], the Ti-22Nb-Hf alloy passivated spontaneously in 0.9% NaCl solution. The I_{corr} and I_{pp} slightly decreased with increasing the Hf contents.

2.2 Titanium oxide surface [28]

TiO_2 is known that a native oxide film grows spontaneously on the surface upon exposure to air. The excellent chemical inertness, corrosion resistance, repassivation ability, and even biocompatibility of Ti and most other Ti alloys are thought to result from the chemical stability and structure of the titanium oxide film that is typically only a few nanometers thick. The composition and oxide thickness of mechanically polished CP-Ti surfaces characterized by X-ray photoelectron spectroscopy (XPS) are summarized in Table 3. The characteristics of films grown at room temperature on pure titanium are schematically shown in Fig. 3 and summarized as follows:

1. The amorphous or nanocrystalline oxide film is typically 3-7 nm thick and mainly composed of the stable oxide TiO_2.

2. The TiO_2/Ti interface has an 0 to Ti concentration ratio that varies gradually from 2 to 1 from the TiO_2 film to a much lower ratio in the bulk.

3. Hydroxide and chemisorbed water bond with Ti cations leads to weakly bound physisorbed water on the surface. In addition, some organic species like hydrocarbons adsorb and metal-organic species, such as alkoxides or carboxylates of titanium also exist on the outmost surface layer whose concentrations depend on not only the surface conditions, such as cleanliness but also the exposure time to air as well as the quality of the atmosphere during storage.

Table 3. Typical XPS oxide film composition and oxide layer thickness of mechanically polished CP-Ti surface [28]

Element	Mechanically polished (at%)	Plus organic solvent (at%)	Plus HNO$_3$ passivation (at%)	Plus O$_2$ plasma (at%)
Ti	14.8 ± 1.6	21.5 ± 1.1	26.1 ± 0.9	27.8 ± 0.8
O	46.8 ± 1.9	51.5 ± 2.0	54.4 ± 2.0	58.8 ± 1.5
C	30.9 ± 2.1	25.1 ± 2.2	19.0 ± 2.9	12.8 ± 1.8
N	0.6 ± 0.2	0.3 ± 0.1	0.5 ± 0.1	0.6 ± 0.2
Si	1.0 ± 0.4	Not detected	Not detected	Not detected
Ca	0.9 ± 0.3	0.2 ± 0.1	Not detected	Not detected
Pb	0.3 ± 0.2	0.3 ± 0.2	Not detected	Not detected
Zn	0.7 ± 0.6	0.6 ± 0.3	Not detected	Not detected
Cu	0.4 ± 0.1	0.5 ± 0.1	Not detected	Not detected
O/Ti atomic ration	2.54 ± 0.14	2.39 ± 0.12	2.08 ± 0.03	2.12 ± 0.04
Oxide layer thickness (nm)	4.3 ± 0.2	4.3 ± 0.2	4.3 ± 0.2	5.1 ± 0.1
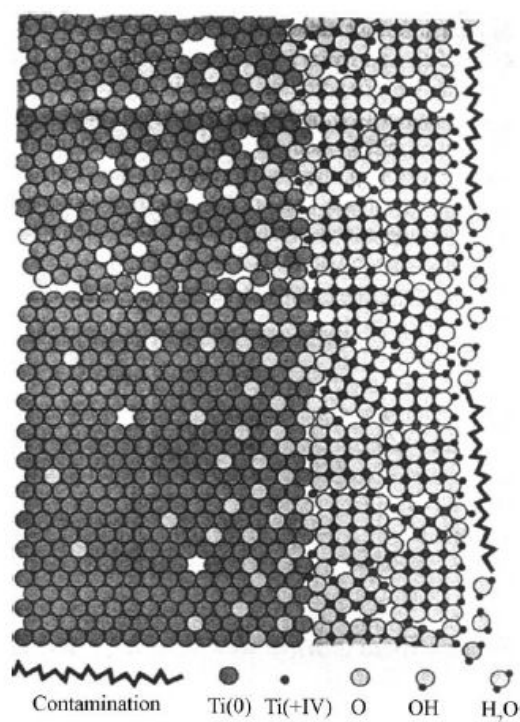
Fig. 3. Schematic view of the oxide film on pure Ti [28].

2.3. Electrochemical anodization process [29]

Anodization is an electrolytic process that creates a protective or decorative oxide film over metallic surface. Anodization increases both the thickness and density of the oxide film. To accomplish it, the conducting piece undergoing anodization is connected to the positive terminal of a de power supply and placed in an electrolytic bath where it serves as the anode. The cathode is commonly a plate or rod of platinum. When power is applied, electrons are forced from the electrolyte to the positive anode. The process leaves surface metal atoms exposed to oxygen ions within the electrolyte. The atoms react and become an in situ integral part of the oxide layer. The electrons travel through the power source and return to the cathode. A depiction of an electrochemical anodization cell is shown in Fig. 4.

Power supply

Ti(anode) → Pt(cathode)
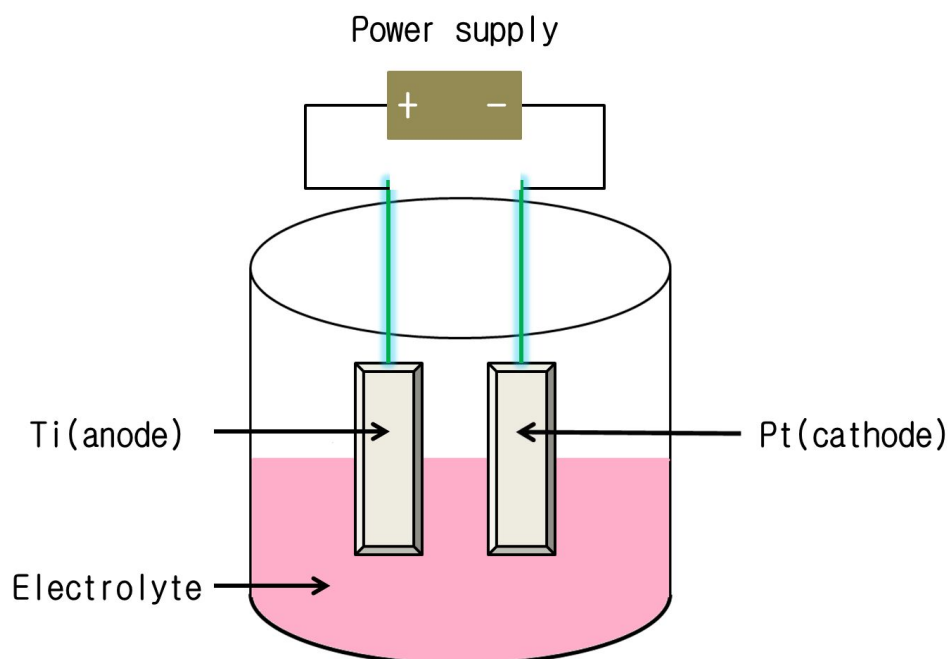
Electrolyte →

Fig. 4. Schematic diagram of a electrochemical cell in which the Ti samples
are anodized [29].

2.4. Microporous oxide formation [30, 31]

The main reactions leading to oxidation at the anode are as follows:
At the Ti/TiO_2 interface:

$$Ti \leftrightarrow Ti^{2+} + 2e^-.$$
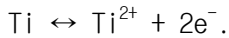
At the TiO_2/electrolyte interface:

$$2H_2O \leftrightarrow 2O^{2-} + 4H^+,$$
$$2H_2O \leftrightarrow O_2 + 4H^+ + 4e^-.$$
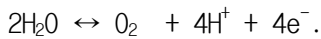
At both interfaces:

$$Ti^{2+} + 2O^{2-} \leftrightarrow TiO_2 + 2e^-.$$

The Ti and oxygen ions formed in these redox reactions are driven through the oxide by the externally applied electric field resulting in the formation of the oxide film. Anodic TiO_2 have high resistivity relative to the electrolyte and the metallic parts of the electrical circuit. The applied voltage drop mainly occurs across the oxide film of the anode. If the anodizing process is carried out at voltages above the breakdown limit, the oxide will no longer be resistive enough to prevent further current flow. At such high voltages, the process will lead to increased gas evolution and frequently sparking. This type of anodizing is often referred to as spark anodizing that typically leads to less uniform and more porous oxide films.

Surgical insertion of many implants such as cortical bone screws and some artificial tooth roots involves significant abrasion. These applications prefer the implant surfaces to have high adherence and surface hardness.

Anodic plasma oxidation of Ti was developed to meet these requirements. When a positive voltage is applied on Ti, it drives Ti atoms to ionize at the metal-oxide interface and oxygen to diffuse through the oxide layer; they combine and the oxide thickens. With the growing oxide thickness, the resistance also increases and this layer takes most of the voltage drop. Surface modification of Ti implants typically uses voltages at hundreds of volts. These are higher than the breakdown voltage of the oxide layer and cause micro-arcs to form locally. The breakdown process creates a local temperature high enough to melt the oxide and an intense O_2 gas evolution. The surface therefore becomes full of crater-like pores. In addition, the micrometer-scale porosity and topography may contribute to the implant fixation by mechanical interlocking.

2.5. Nanotube formation mechanism [32]

It is generally agreed that TiO_2 nanotubes form in F^- containing electrolytes by two competing electric field-assisted processes (Fig. 5). The first process involves the active dissolution of the Ti metal to form a passive TiO_2 layer:

$$Ti + 2H_2O \rightarrow TiO_2 + 4H^+ + 4e^- \quad (1)$$
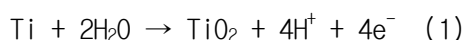
The second process is related to the chemical dissolution of the newly formed oxide by the following reaction:

$$TiO_2 + 4H^+6F^- \rightarrow [TiF_6]^{2-} + 2H_2O \quad (2)$$

The evolution of the TiO_2 microstructure can be described by four stages which are shown schematically in Fig. 6 and described below;

1st step:
The initial steps of anodization are characterized by a large decrease in the current density with time due to the formation of a dense oxide layer by the dissolution of Ti (Eq. (1)). In the absence of F^- the growth of the oxide is self-limiting and eventually the current density and thickness stabilize at a constant value.

2nd step:
In the presence of F^-, chemical dissolution of TiO_2 is possible, as described by Eq. (2). Thus, 2nd step is characterized by the formation of nanopores across the surface of the TiO_2 layer. Pore formation is driven by local dissolution of TiO_2, which reduces the film thickness, locally, and increases the electric field intensity at the bottom of the pore. The

increased current density drives the formation of new oxide at the metal/oxide interface while also increasing the rate of chemical dissolution at the oxide electrolyte interface.

3rd step:

As the nanopores continue to grow into the oxide layer there is an abrupt transition from nanopores to nanotubes. As a result, 3rd step is characterized by the presence of a bi-layered structure. The top layer consists of the nanoporous region and the bottom layer consists of the nanotube layer. During this step, nanotubes grow deeper into the substrate due to the competition of oxide growth and dissolution at the bottom of the nanotube. As nanotubes continue to grow, the nanoporous layer is subjected to chemical dissolution, resulting in thinning and eventual disappearance. As the thickness of the oxide layer increases, the current density decreases. The mechanistic explanation for the transition from nanopores to nanotubes is somewhat unclear. Thus, by this proposed mechanism, the nanotubes are the result of simultaneous growth of gaps and pores.

4th step:

Once the nanoporous layer has undergone complete dissolution the coating consists of an ordered array of TiO$_2$ nanotubes. With continued anodization the nanotubes continue to grow in length, and the current density continues to drop, until the so-called "equilibrium thickness" is established and both the current density and coating thickness stabilize.
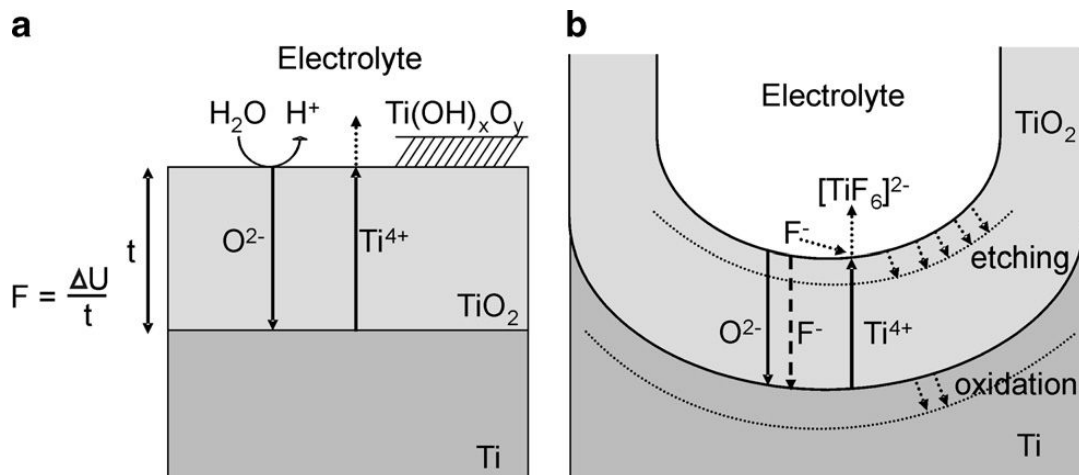
Fig. 5. Schematic representation of the Ti anodization (a) in absence of fluorides (results I flat layers) and (b) in presence of fluorides (result in the tube growth) [33].
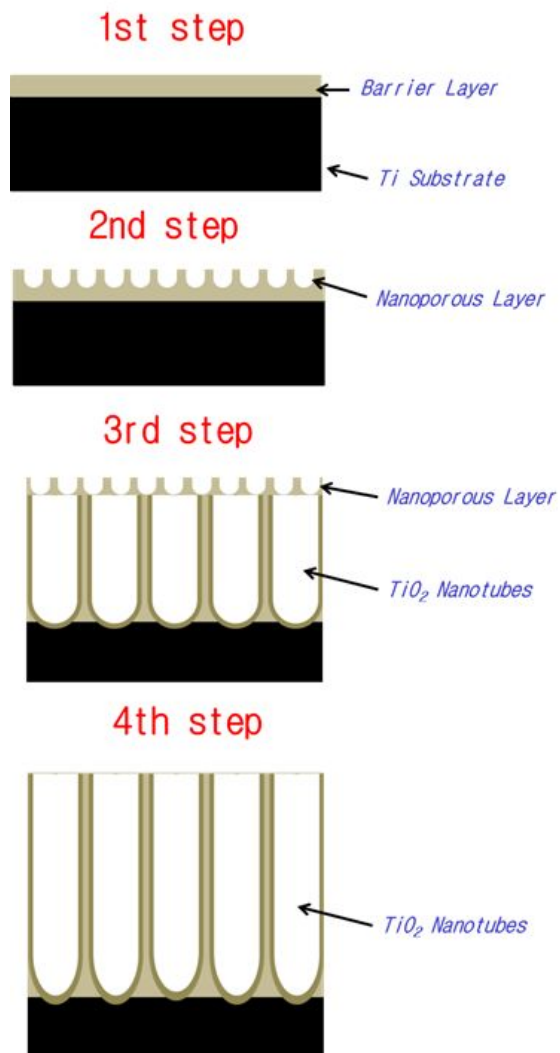
Fig. 6. Schematic diagrams showing the mechanism for TiO₂ nanotube formation [32].

III. MATERIALS AND METHODS

3.1. Ti-25Nb and Ti-25Nb-7Hf alloy preparation

The Ti-25Nb and Ti-25Nb-7Hf alloys were prepared using CP Ti (G&S Titanium, Grade 4, USA), Nb, and Hf (Kurt J. Lesker Company, 99.95 wt.% purity, USA). All materials were cleaned by ultrasonic cleaner in acetone and dried in air.

The Ti-25Nb and Ti-25Nb-7Hf alloys were prepared by using the vacuum arc melting furnace. The weighed charge materials were prepared in the vacuum arc furnace (vacuum arc melting system, SVT, KOREA), the high-purity Ar gas was filled up to water cooling copper hearth chamber in vacuum atmosphere of 0.133 Pa. The atmosphere in chamber was controlled by method to keep vacuum by fine gage. The Ti-25Nb and Ti-25Nb-7Hf alloys ingots were remelted at least 10 times in order to avoid inhomogeneity. The ingots of Ti-25Nb and Ti-25Nb-7Hf alloys were homogenized in Ar atmosphere at 1000 ℃ (MSTF-1650, MS Eng, KOREA) for 12h and then, 0 ℃ water quenching. The ingots were cut off by diamond wheel cutting system (Accutom-5, Struers, Denmark) by way of a thickness of 2.5 mm for experiments, and then ultrasonically cleaned in acetone and finally dried in air.

3.2. Analysis of surface characteristics for the alloy

The phase and composition of the Ti-25Nb and Ti-25Nb-7Hf alloys were determined by using X-ray diffractometer (XRD, X`pert PRO, Philips). Ni-filtered Cu Kα radiation was used in this study. Phase was identified by matching each characteristic peak with JCPDS files. The Ti-25Nb-7Hf alloy, micro-pore and nanotube formed surfaces were observed by optical microscopy (OM, oympus, BX 60M, Japan), field-emission scanning electron microscopy (FE-SEM, Hitachi, 4800, Japan), X-ray diffractometer (XRD, X`pert PRO, Philips), and energy dispersive x-ray spectroscopy (EDS, Oxford ISIS 310, England). The etching treatment was performed in Keller's reagent (2 ml HF + 3 ml HCl + 5 ml HNO$_3$, + 190 ml H$_2$O).

3.3. Micro-pore formation on the alloy surface

Anodization treatments on Ti-25Nb and Ti-25Nb-7Hf alloys were carried out in electrolyte containing 1M H_3PO_4 at room temperature for experiments. The electrolyte was stirred surfing anodizing process, anodization was carried out using by DC power supply (KDP-1500, KOREA) at 200 V for 3 min. The current density during anodizing process was 0.25 A/cm^2 and counter electrode was platinum. The morphology of the porous Ti oxide was characterized by a FE-SEM, EDS, and XRD. To measure the fraction of surface precent for pores and pore walls from FE-SEM image of micro-pore formed the alloy, the Image J (http://rsb.info.nih.gov/ij/, NIH, USA) software and image analyzer (Image Pro Plus, Media Cybernetics, PA, USA) was applied.

(a) DC power supply
(b) Voltage controller
(c) Hot plate
(d) Stirrer
(e) Cathode: platinum
(f) Anode: sample
(g) Electrolyte
(h) Stirrer speed controller
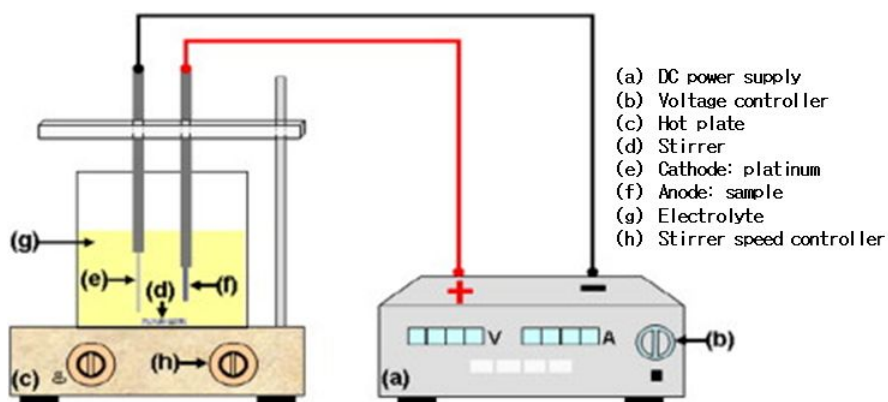
Fig. 7. Schematic diagram of the apparatus for anodizing.

3.4. Nanotube formation on the alloy surface

The electrochemical experiment consisted of two electrode configuration with platinum as the counter electrode and the working electrode as anode was used for anodization. The samples was embedded in epoxy resin, leaving a square surface area of 10mm^2 exposed to a 1M H_3PO_4 electrolytes containing 0.8 wt. % NaF as anodizing electrolyte. All nanotube formation experiments were carried out at constant potential (20 ~ 40 V) for (30 ~ 120) min (potentiostat 362, EG&G Company, USA). After the anodization, the samples were rinsed in distilled water and subsequently in acetone, and dried in air. The morphology of the nanotube formation on the alloy surface characterized by a FE-SEM.

3.5. Micro-pore and nanotube formation on the alloy surface

The electrochemical experiment consisted of a two electrode configuration with platinum as the counter electrode and the working electrode as anode was used for anodization. Micro-pore and nanotube formation of Ti-25Nb-7Hf alloy was carried out in each different solution at room temperature by two step anodization method. Micro-pore formation was performed in 1M H_3PO_4 electrolytes at 200 V at 3 min, and then nanotube formation was carried out in 1M H_3PO_4 electrolytes containing 0.8 wt. % NaF at 30 V 120 min. After the anodization treatments, the samples were rinsed in distilled water and subsequently in acetone, and dried in air. The morphology of the micro-pore and nanotube formation on the alloy surface characterized by a FE-SEM, EDS, and scanning transmission electron microscope (STEM, JEM-2100F, JEOL, Japan).

3.6. Corrosion test of the alloy surface

Corrosion behaviors were investigated using a standard three-electrode cell having the specimen as a working electrode and a high dense carbon counter electrode. The potential of the working electrode was measured against a saturated calomel electrode (SCE) and all specimen potentials were referenced to this electrode. The corrosion properties of the samples were first examined by a potentiodynamic polarization test (scanning range from -1500 to 2000 mV) at scan rate of 1.667 mV/s in 0.9 % NaCl electrolyte at 36.5 ± 1 ℃. (PARSTAT 2273, EG&G Company, USA). Using an automatic data acquisition system, the potentiodynamic polarization curves were plotted and both corrosion rate and potential were estimated by tafel plots by using both anodic and cathodic branches. The conditions of electrochemical corrosion test were shown in Table 4.

Table 4. The conditions of electrochemical corrosion test

	Potentiodynamic test
Working electrode	Samples
Reference electrode	Saturated calomel electrode
Counter electrode	High dense carbon
Electrolyte	0.9% NaCl
Working temperature	36.5 ± 1 ℃
Gas purging	Ar gas
Scan rate	1.667 mV/sec
Scanning range	-1500 ~ +2000 mV

3.7. Wettability test of the alloy surface

Surface wettability test was performed on the surface and anodized surface using a water contact angle goniometer (Kruss DSA100, Germany) in sessile drop mode with 5 $\mu\ell$ drops.

Ⅳ. RESULTS AND DISCUSSION

4.1. Microstructures of Ti-25Nb and Ti-25Nb-7Hf alloys

Fig. 8 shows the microstructures of the Ti-25Nb-xHf alloys with different Hf content (0 wt.% and 7 wt.%) after homogenization treatment at 1000 ℃ for 12 h in argon atmosphere and then water quenching. The Ti-25Nb binary alloy had only needle-like martensitic structure with α" phase as shown in Fig. 8 (a) [34]. It was corresponded with previous research results; the Ti-Nb alloys with 17.5 wt.% ~ 25 wt.% Nb were the primarily comprised an orthorhombic α" phase [25]. But, the Ti-25Nb-7Hf alloy have less needle-like trace than Ti-25Nb alloy surface and showed equiaxed structure with β phase in Fig. 8 (b) [34]. This means, Ti-25Nb-xHf alloy surface could be suppressed occurring of metastable phase like an α" by addition of Hf contents, which could be act as a β phase stable element [5, 16].

Fig. 9 shows the XRD patterns of Ti-25Nb-xHf alloys. All kind of peaks were identified by referring to the JCPDS file. The Ti-25Nb alloy showed only orthorhombic α" phase crystal structure whereas the Ti-25Nb-7Hf alloy showed α"+ β phases as shown in XRD patterns of Fig. 9. These results could be confirmed with FE-SEM images from Fig. 8 (a) and (b) which was composed of needle-like martensitic structures of α" phase on binary Ti-25Nb alloy but Ti-25Nb-7Hf alloy showed equiaxed structure of β phase. It is assumed that the addition of Hf element also suppresses the precipitation of the metastable α" martensitic phase and stabilized the β phase during the water quenching process [27].
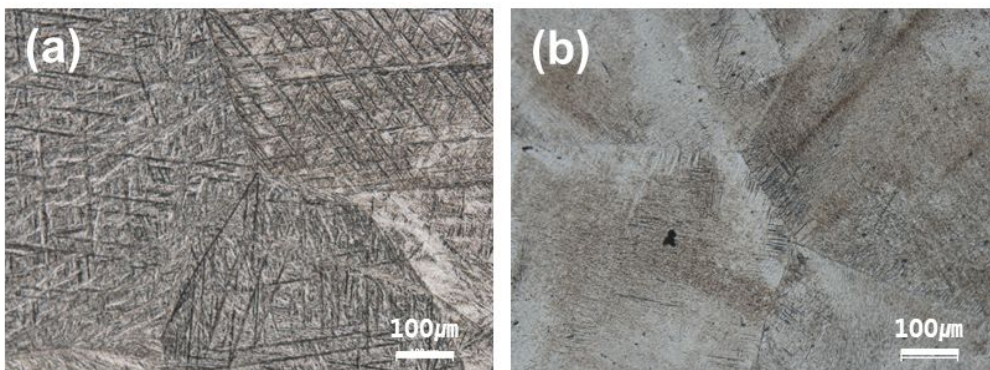
Fig. 8. OM images showing Ti-25Nb-xHf alloys after heat treatment at 1000 ℃ for 12 h in Ar atmosphere and then, 0 ℃ water quenching: (a) Ti-25Nb (b) Ti-25Nb-7Hf.
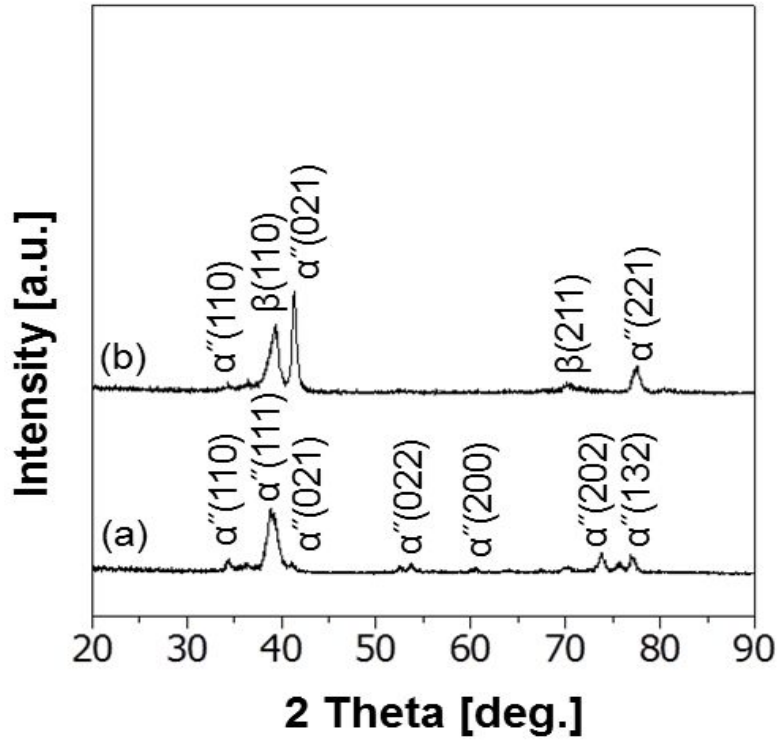
Fig. 9. XRD peaks of Ti-25Nb-xHf alloys after heat treatment at 1000 ℃ for 12 h in Ar atmosphere, followed by 0 ℃ water quenching: (a) Ti-25Nb (b) Ti-25Nb-7Hf [34].

4.2. The micro-pore surface morphologies of Ti-25Nb and Ti-25Nb-7Hf alloys

Fig. 10 shows the voltage-time and current-time displacement for micro-pore forming of Ti-25Nb-xHf alloys. The oxide film formation was performed by anodic oxidation on Ti-25Nb and Ti-25Nb-7Hf alloy, for which, the voltage initially decreased, whereas current decreased for 10sec, but, it swiftly increased to setting range of 200 V, it could be maintained with constant voltage. Whereas, the current initially decreased from 25 mA/cm^2 to close of 0.25 mA/cm^2, but, it was having a arrhythmic transform to act or not act which due to dielectric breakdown of the oxide films with anodic spark depositions at high voltages [35]. There was no differences for applying current between the Ti-25Nb and Ti-25Nb-7Hf alloy.

Fig. 11 shows the surface morphology and chemical composition of micro-pore formed Ti-25Nb and Ti-25Nb-7Hf alloy. Anodization treatment was performed at 200 V for 3 min on the Ti-25Nb and Ti-25Nb-7Hf alloys. The porous oxide layers were formed as shown in Fig. 11 (a), (b). Well fabricated pores were distributed homogeneously over the surface of both alloys as shown in Fig. 11. (a), (b) and the pore sizes of Ti-25Nb and Ti-25Nb-7Hf alloy were around 500 nm and 1 μm for respectively. That is, the number of micro-pore decreased with presence of Hf content added, whereas, the size of micro-pore increased with presence of Hf content added. And it was confirmed from chemical composition of oxide layer by EDS analysis. It was considered that the oxide films on Ti-25Nb and Ti-25Nb-7Hf alloy were composed of the alloying elements including oxygen [35].

Fig. 12 shows images analysis results of Fig. 11 (a) and (b). The occupied pore ratio (white color) on the TiO$_2$ layer. The results of the analyses are listed in Table 5, which shows that the fraction of the surface area occupied by pores decreases with added Hf content, with a corresponding increase in the fraction of surface area occupied by the pore walls,

slightly. Also, the number of pores decrease with added Hf content from 26 / μm^2 to 14 /μm^2. These results indicate that due to corrosion resistance of the alloy increase with Hf content added [11].

Fig. 13 shows the phase structures of micro-pore formed Ti-25Nb-xHf alloys were analyzed by XRD. Fig. 13 (a) shows the peaks from Ti-25Nb alloy, and Fig. 13 (b) shows peaks from Ti-25Nb-7Hf alloy, respectively. From the Ti peaks, the peaks were similar with non micro-pore formed surface as shown in Fig 9, which have α'' and β phase for Ti-25Nb and Ti-25Nb-7Hf alloys, respectively. While the peaks of TiO_2 consisted predominantly of anatase with small amount of rutile, which was mixture showed on the micro-pore formed surface of Ti-25Nb and Ti-25Nb-7Hf alloys. Regarding with this result, the amount of the anatase phase is considered to have a role in the efficient nucleation and growth of hydroxyapatite compared with the rutile phase because of its better lattice match with hydroxyapatite [35, 36, 37].
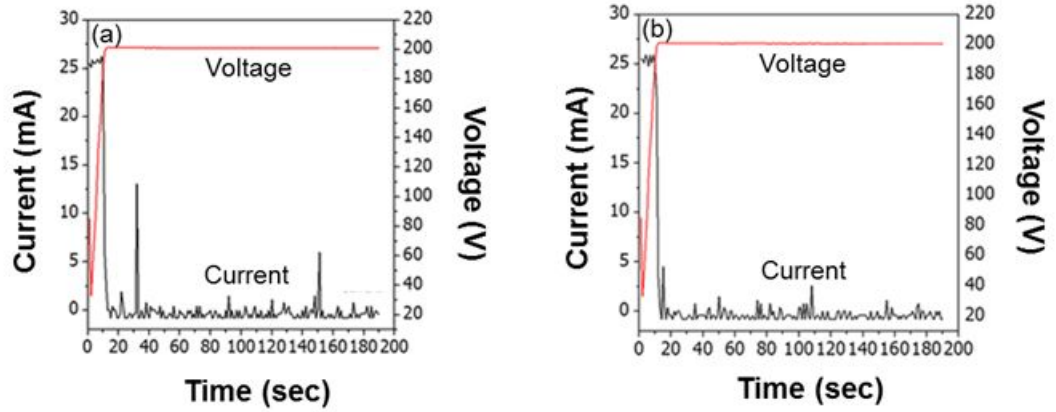
Fig. 10. Voltage-time and current-time displacement for micro-pore forming
of Ti-25Nb-xHf alloys: (a) Ti-25Nb and (b) Ti-25Nb-7Hf [34].
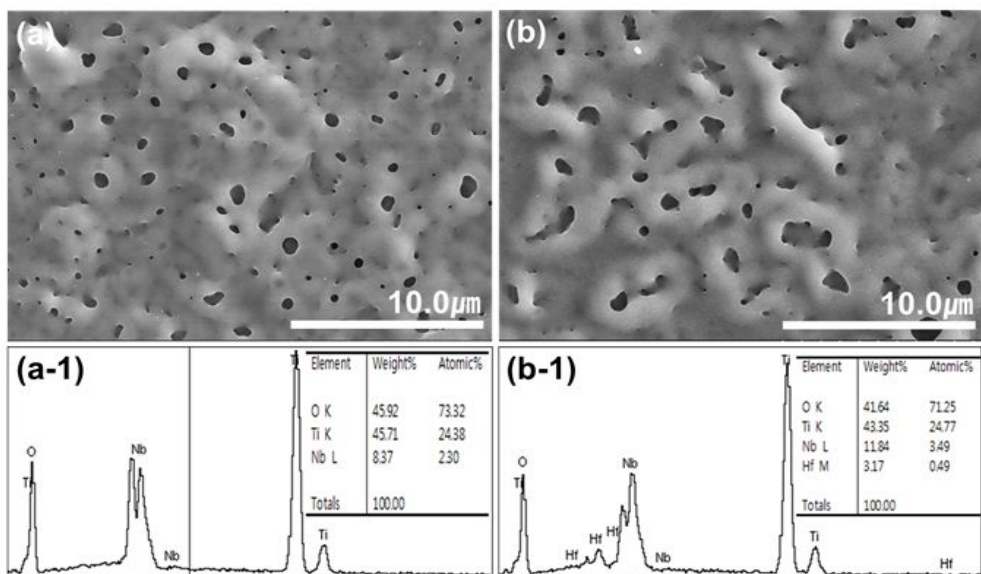
Fig. 11. FE-SEM images and EDS analysis showing micro-pore formed on Ti-25Nb-xHf alloys by anodization in 1M H_3PO_4 at 200 V for 3 min: (a) Ti-25Nb and (b) Ti-25Nb-7Hf; chemical composition on anodized (a-1) Ti-25Nb and (b-1) Ti-25Nb-7Hf.
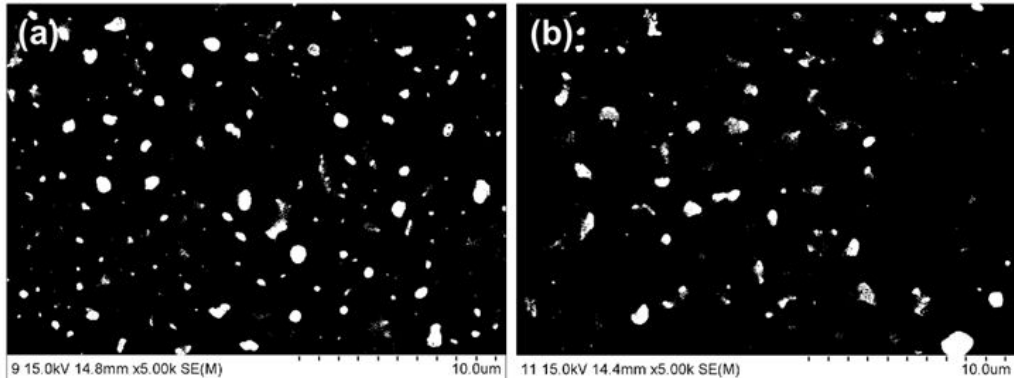
Fig. 12. Images analysis results of Fig. 11 (a) and (b): (a) Fig. 11(a) and (b) Fig. 11(b).

Table 5. The fraction of surface area percent for pores and pore walls of
micro-pore formed on the alloys

samples	Fraction of area occupied by pores (%)	Fraction of area occupied by pore walls (%)	Number of pores ($/\mu m^2$)
Ti-25Nb	10.33	89.67	26
Ti-25Nb-7Hf	9.17	90.83	14

Fig. 13. XRD peaks of micro-pore formed Ti-25Nb-xHf alloys by anodization in 1M H_3PO_4 at 200 V for 3 min: (a) Ti-25Nb and (b) Ti-25Nb-7Hf [34].

4.3. The nanotube surface morphologies of Ti-25Nb and Ti-25Nb-7Hf alloys

Fig. 14 shows the nanotubes morphologies of Ti-25Nb and Ti-25Nb-7Hf alloys in electrolyte containing 1 M H_3PO_4 + 0.8 wt. % NaF for 1 h at applied anodic potential of 30V.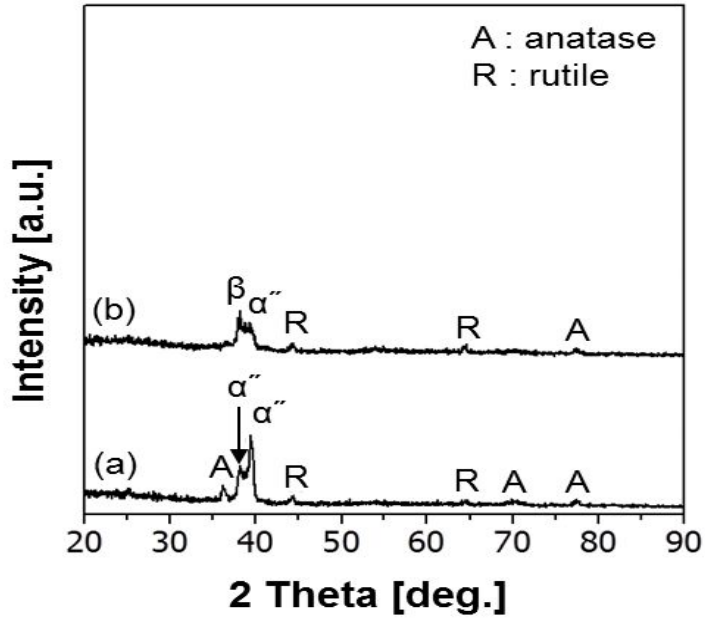 FE-SEM images are showing the nanotubular top, bottom, and cross-section as shown in Fig. 14 (a, b, c) for Ti-25Nb and Fig. 14 (d, e, f) for Ti-25Nb-7Hf alloy, respectively. At the bottom of the alloys, the smaller nanotubes appeared and more regularly arranged as the Hf contents increased in Fig. 14 (b) and (e). As the Hf content added, the average length of the nanotubes increased in the order of approximately 3 μm and 3.25 μm in Fig. 14 (c) and (f). It is evident that the nanotube thickness could be controlled by Hf content in the Ti-25Ta-xHf alloys. From previous report by Choe et al. [14, 15], ZrO_2 and Ta_2O_5 films on the Ti-Ta-Zr alloy can hold off their growth in NaF contained electrolyte. It is considered that the two sized nanotubes were formed in F^-ion contained electrolyte on the Ti-25Nb-xHf alloys with increasing of Hf contents. These results indicate to have these phenomena with the reason of the HfO_2 formation on the nanotube films. These investigations can be suggested that Hf has a role in the formation of a stable film that resists to be attacked from the F^-ion which has devoid of nanotubes formation as subsequent nucleation sites for the smaller tubes [38].

Fig. 15 and Fig. 16 shows FE-SEM images of cross-section of nanotube and the variation of nanotube thickness with anodization on the Ti-25Nb-7Hf alloy at different times in 1M H_3PO_4 + 0.8 wt.% NaF at 30 V. The thickness of the nanotube layers increased from about 0.75 μm to 4 μm, when the anodization time was increased from 30 min to 120 min. The thickness of the nanotube layers could also be varied by changing the anodization time. From previous report by Kim et al. [15], the thickness of the nanotube layer on Ti-35Ta-15Zr gradually increased with increasing anodization time from 4 μm

to 9.5 μm. This means that the process of nanotube growth was governed by competition between anodic oxide film formation and chemical dissolution of the oxide by F$^-$ ion. It is consistent that the thickness of the nanotube layers increased with time in our study.

Fig. 17 and Fig. 18 shows FE-SEM images of cross-section of nanotube and the variation of small and large diameter of nanotube on the Ti-25Nb-7Hf alloy at different potentials in 1M H_3PO_4 + 0.8 wt.% NaF for 1h. As the applied potential increased, the small nanotubes were more irregularly arranged and diameters of small and large nanotubes increased compared with nanotube formed at low applied potential. Generally, if the applied potential increased, the diameter of the ordered nanotubes on surface increased [15]. By the controlled the applied potential, the diameter of the nanotube layers could be controlled for improving tissue adhesion.
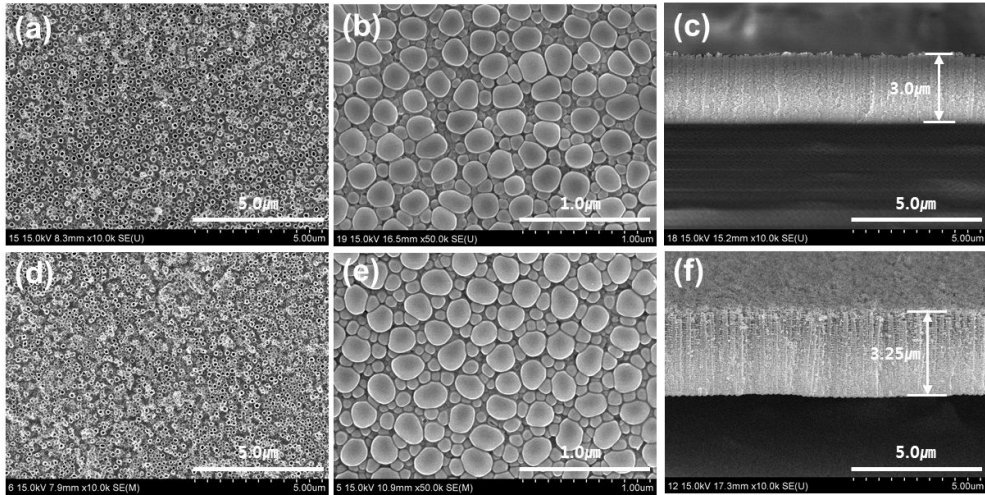
Fig. 14. FE-SEM images showing the top, bottom and cross-section view of nanotube on (a, b, c) Ti-25Nb and (d, e, f) Ti-25Nb-7Hf alloy in 1M H_3PO_4 + 0.8 wt.% NaF for 1h at 30V.
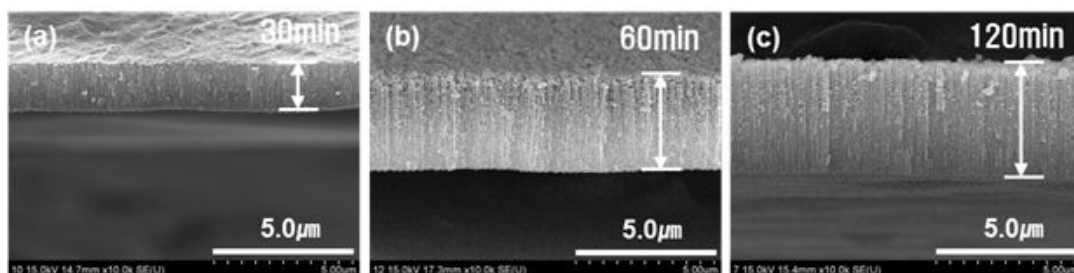
Fig. 15. FE-SEM images showing cross-section of nanotube on the Ti-25Nb-7Hf
  alloy at different times in 1M H_3PO_4 + 0.8 wt.% NaF at 30V.
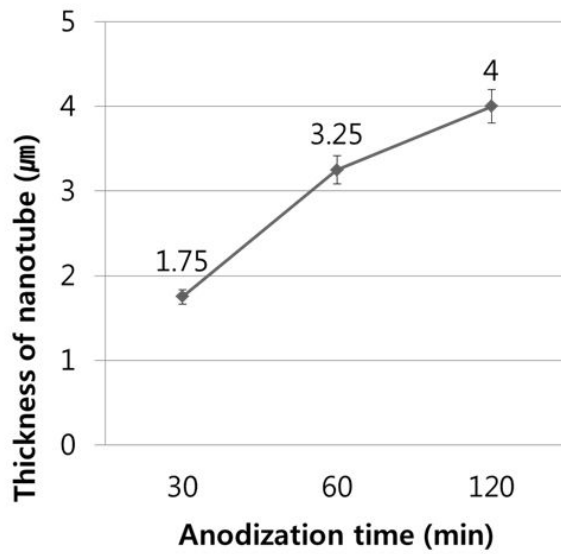
Fig. 16. The variation of nanotube thickness with anodization on the Ti-25Nb-7Hf alloy at different times in 1M H3PO4 + 0.8 wt.% NaF at 30V.
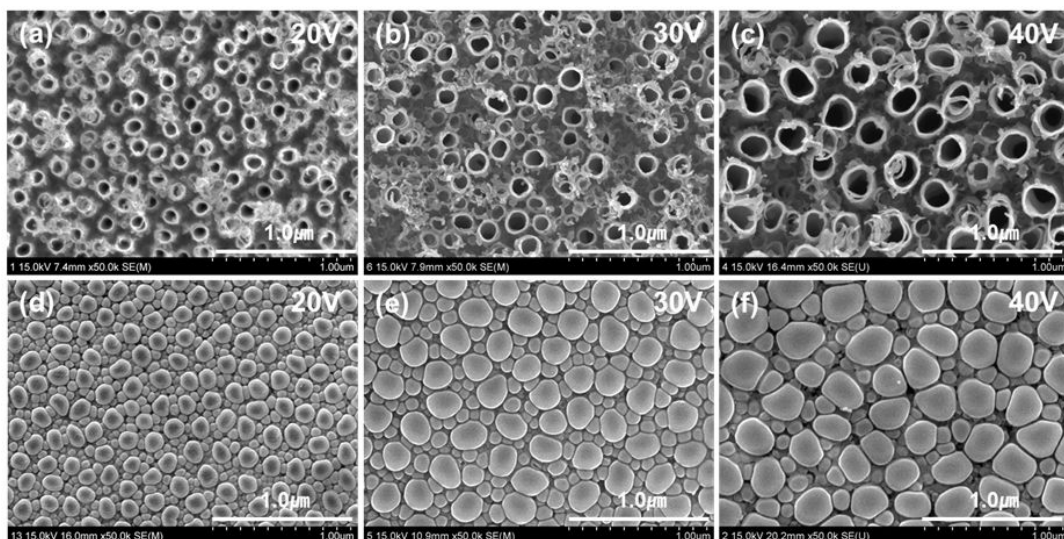
Fig. 17. FE-SEM images showing top (a, b, c) and bottom (d, e, f) view of nanotube on the Ti-25Nb-7Hf alloy at different potentials in 1M H_3PO_4 + 0.8 wt.% NaF for 1h.

Fig. 18.The variation of small and large diameter of nanotube on the Ti-25Nb-7Hf alloy at different potentials in 1M H_3PO_4 + 0.8 wt.% NaF for 1h.

4.4. The micro-pore and nanotube surface morphologies of Ti-25Nb and Ti-25Nb-7Hf alloys

Fig. 19 shows FE-SEM images of nanotube formed in the micro-pore on Ti-25Nb and Ti-25Nb-7Hf alloy. The micro-pore and nanotube were well formed on the alloy surface by two step anodization method as shown in Fig. 19 (a) and (d). Especially, nanotubes were formed in the micro-pore as shown in Fig.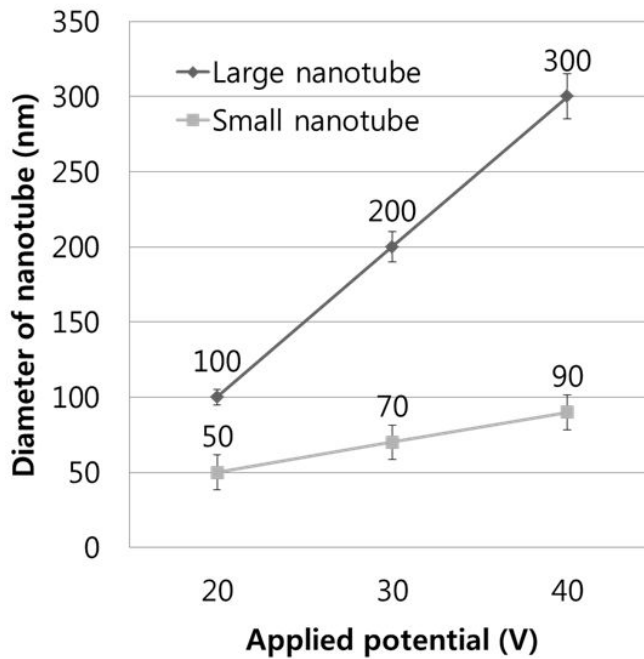 19 (c) and (f), but, nanotubes were not formed on Ti oxide surface. The multi structures with various sizes from micro to nano were obtained through two step anodization surface treatment. From previous report by Jiang et al. [39], in vitro apatite formation was an important sign to evaluate the bioactivity of biomedical implants. These results of apatite precipitation showed that the surface with a micro/nano-network structure possessed the best ability of biomineration. Therefore, we confirm that surface morphology structures with micro-pore and nanotube formed by two step anodization can improve the biomineration and bioactivity of implant.

Fig. 20 shows STEM and EDS peaks of micro-pore and nanotube formed Ti-25Nb alloy. It was confirmed that nanotube was formed in the area of micro-pore formation from cross-sectioned image (STEM) and EDS analysis results. Also, the thickness of anodization was about 4 μm.

Fig. 21 shows FE-SEM images of porous surface formed Ti-25Nb-7Hf alloy at edge area of micro-pore. The nanotube was formed in the area of micro-pore formation, whereas, nanotube was not formed on the one step anodized surface without micro-pore in Fig. 21. This means that the mixed (TiO_2 + Nb_2O_5 + HfO_2) oxide layer by anodization for micro-pore formation is more stable than TiO_2 oxide layer [14, 38].
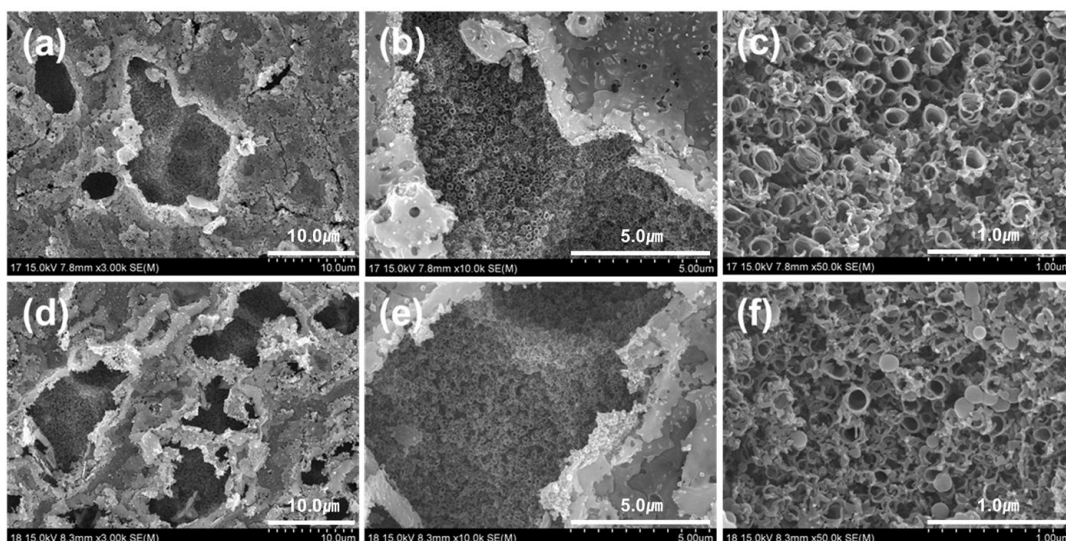
Fig. 19. FE-SEM images showing nanotube formed in the micro-pore on Ti-25Nb-xHf alloys : (a, b, c) Ti-25Nb and (d, e, f) Ti-25Nb-7Hf.

Spectrum	In stats.	O	F	Ti	Nb	Total
1	Yes	31.53	2.31	48.66	17.51	100.00
2	Yes	25.39	0.00	51.51	23.09	100.00
3	Yes	23.44	0.00	55.17	21.39	100.00
4	Yes	27.42	2.56	46.86	23.16	100.00
5	Yes	22.75	1.57	49.93	25.75	100.00
6	Yes	22.65	2.56	51.70	23.09	100.00
7	Yes	1.04	0.00	71.45	27.51	100.00

Fig. 20. STEM and EDS peaks showing micro-pore and nanotube formed on the Ti-25Nb alloy.

Fig. 21. FE-SEM images showing porous surface formed Ti-25Nb-7Hf alloy at edge area of micro-pore.

4.5. Electrochemical characteristics of the alloy with surface treatments

Fig. 22 shows the potentiodynamic polarization curves of Ti-25Nb-7Hf alloy with various surface treatments in 0.9% NaCl solution at 36.5 ± 1 ℃. The results of corrosion potential (E_{corr}), corrosion current density (I_{corr}), and current density at 300 mV (I_{300mV}) and primary passivation potential (E_{pp}) from the potentiodynamic polarization curve are given in Table 6. In case of micro-pore formed Ti-25Nb-7Hf alloy surface, E_{corr} value is -560 mV and I_{corr} value is 2.81×10^{-7} A/cm^2. The E_{corr} decreased from -400 mV to -560 mV and also I_{corr} decreased slightly from 9.06×10^{-7} A/cm^2 to 2.81×10^{-7} A/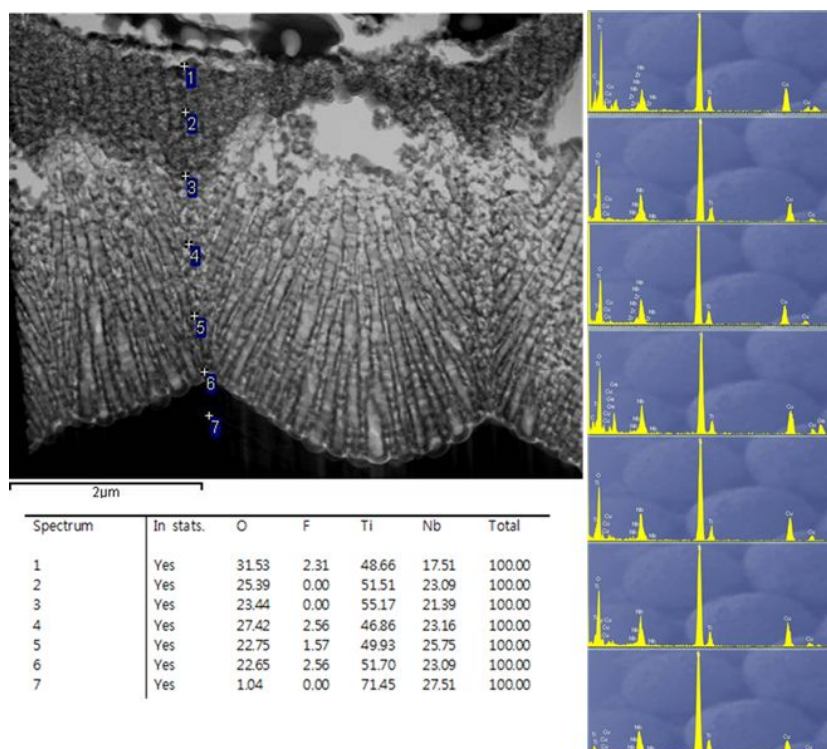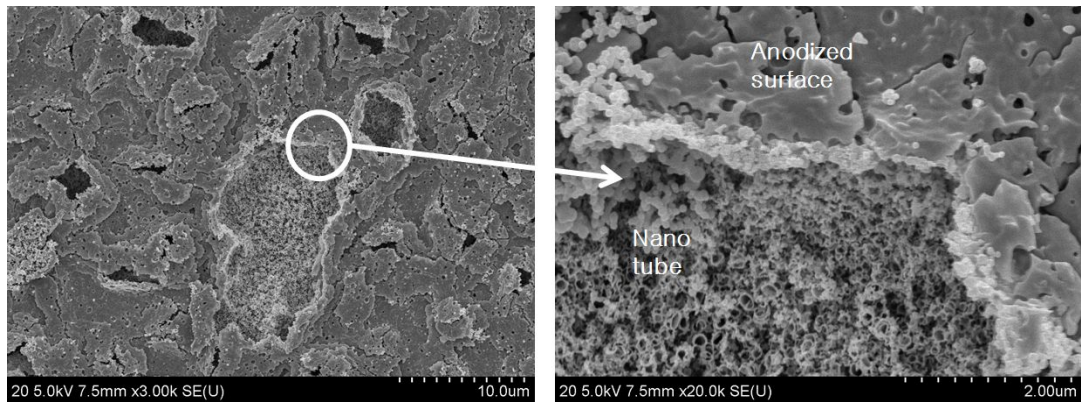cm^2 compared with bulk surface. It is confirmed that porous surface serves the corrosive sites and increases dissolution rate in 0.9% NaCl electrolyte [40]. And the passive region of micro-pore surface shifted from the right side to the left side compared with bulk surface. It is thought that the thick oxide film plays role in inhibitor against corrosive chloride ions in the electrolyte [40]. In case of micro-pore and nanotube formed Ti-25Nb-7Hf alloy surface by two step anodization, E_{corr} value is -750 mV and I_{corr} value is 1.08×10^{-5} A/cm^2. the E_{corr} decreased from -400 mV to -750 mV and I_{corr} increased from 9.06×10^{-7} A/cm^2 to 1.08×10^{-5} A/cm^2 compared with bulk surface. However, the E_{PP} value of micro-pore and nanotube formed the alloy surface by two step anodization showed lowest (-430 mV) rather than those of bulk and micro-pore surfaces. Also, the passive region of micro-pore and nanotube formed the alloy surface by two step anodization showed more stable and wider compared with bulk surface. It is thought that ion release is occurred in micro-pore and nanotube formed surface area by two step anodization compared with bulk surface [37, 38].
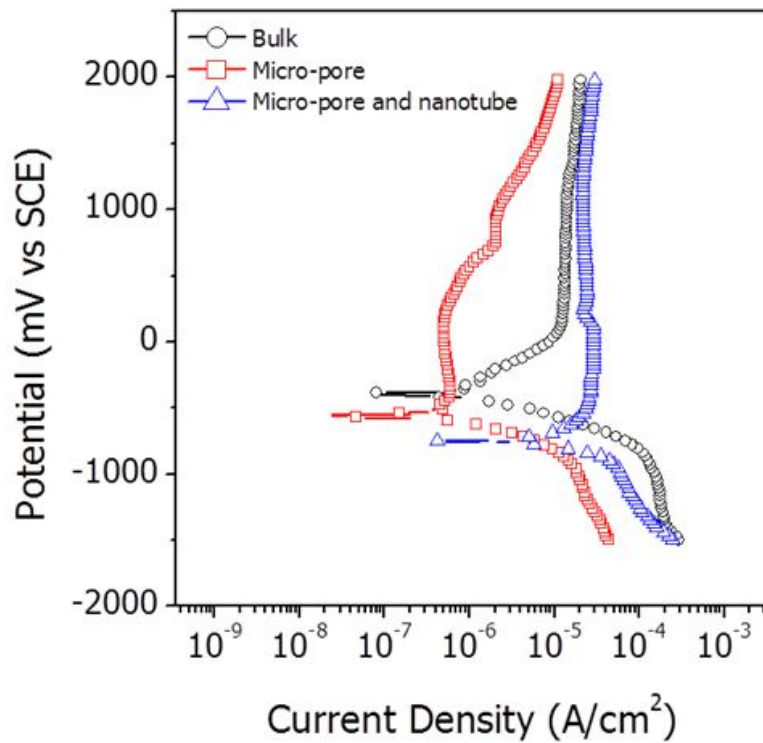
Fig. 22. Potentiodynamic polarization curves of Ti-25Nb-7Hf alloy with surface treatments.

Table 6. Corrosion potential (E_{corr}), current density at 300 mV (I_{300mV}), corrosion current density (I_{corr}), primary passivation potential (E_{pp}), of Ti-25Nb-7Hf alloy with surface treatments from potentiodynamic test

	E_{corr} (mV)	I_{300mV} (A/cm^2)	I_{corr} (A/cm^2)	E_{pp} (mV)
Bulk	−400	1.30×10^{-5}	9.60×10^{-7}	10
Micro-pore	−560	5.86×10^{-7}	2.81×10^{-7}	−470
Micro-pore and nanotube	−750	2.34×10^{-5}	1.08×10^{-5}	−540

4.6. Wettability of the alloy with various surface modification

Fig. 23 shows contact angles as an indication of surface wettability and surface biocompatibility with different surface treatment. In Fig. 23 (a) and (d), the contact angles are average 31 ± 2° and 25 ± 2°, respectively. Fig. 23 (b) and (e) shows the improved wettability, and reduce significantly the contact angles, (average 7 ± 2° and 10 ± 2°) due to micro-pore formation. Fig. 23 (c) and (f) shows slightly the lower value of average 2.4 ± 2° and 3.1 ± 2° compared with Fig. 23 (b) and (e) due to micro-pore and nanotube formation by two step anodization. Therefore, micro-pore formed oxide surface and micro-pore and nanotube formed oxide surface shows a hydrophilic behavior, due to complete spreading of water on the entire and into the pores [16, 41, 42].
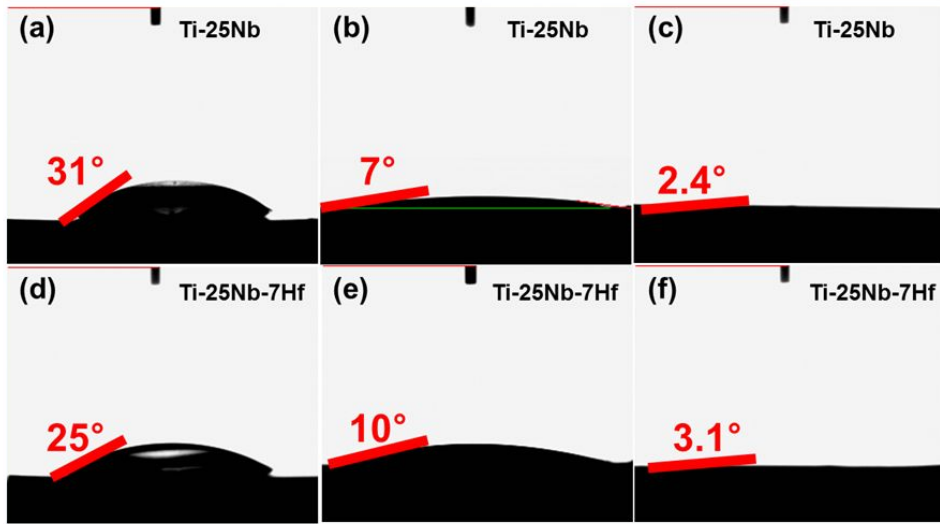
Fig. 23. Contact angle measurements of Ti-25Nb and Ti-25Nb-7Hf surfaces: (a, d) non treated, (b, e) micro-pore formed, (c, f) micro-pore, and nanotube formed.

Ⅴ. CONCLUSIONS

In this study, surface characteristics of the micro-pore and nanotube formed Ti-25Nb-7Hf alloy by two step anodization have been researched.

The results were as follows;

1. Microstructures of the alloys were transformed form α″ phase to β phase, and a needle-like to an equiaxed structure as Hf content added. The Ti-25Nb alloy showed only orthorhombic α″ phase whereas, the Ti-25Nb-7Hf alloy showed α″+ β phases.

2. The peaks of anatase and rutile showed on the micro-pore surface of the alloys. The number of micro-pore decreased as Hf content added, whereas size of micro-pore increased.

3. The diameter of the nanotube increased, as the applied potential increased. As the Hf content added, the average length of the TiO_2 nanotubes increased and nanotubes were more regularly arranged. As anodization time increased, the nanotube thickness increased.

4. Nanotube was formed in micro-pore, but, not formed on the area of non-formed micro-pore.

5. Micro-pore and nanotube formed Ti-25Ta-7Hf alloy showed lower E_{corr} and higher I_{corr} than those of bulk and micro-pore surfaces.

6. Contact angle of micro-pore and nanotube formed surface showed lower than those of bulk and micro-pore surface.

In conclusion, it is concluded that micro-pore and nanotube formed on the Ti-25Nb-7Hf alloy by two step anodization have arrays of micro and nano structure. Therefore, surface morphology of micro-pore and nanotube structure by two step anodization can enhance the osseointegration and cell adhesion.

- Reference -

1. M. A. Khan, R. L. Williams, D. F. Williams, Biomaterials 20 (1999) 631.

2. D. M. Brunette, P. Tengvall, M. Textor, P. Thomsen, Titanium in Medicine, Springer, Berlin, 2001.

3. H. C. Choe, W. G. Kim, Y. H. Jeong, Surf. Coat. Technol. 205 (2010) S305.

4. B. H. Moon, Y. H. Jeong, H. C. Choe, J. Nanosci. Nanotechnol. 11 (2011) 7428.

5. J. U. Kim, Y. H. Jeong, H. C. Choe, Surf. Interface Anal. 44 (2012) 1468.

6. R. Zhang, V. L. Acoff, Mater. Sci. Eng. A 463 (2007) 67.

7. A. L. Yerokhin, X. Nie, A. Leyland, A. Matthews, S. J. Dowey, Surf. Coat. Technol. 122 (1999) 73.

8. X. Liu, P. K. Chu, C. Ding, Mater. Sci. Eng. R 47 (2004) 49.

9. T. H. The, A. Berkani, S. Mato, R. Skeldon, G. E. Thompson, H. Habazaki, K. Shimizu, Corroso. Sci. 45 (2003) 2757.

10. T. Kakubo, Acta Mater. 46 (1998) 2519.

11. T. E. Park, H. C. Choe, W. A. Brantley, Surf. Coat. Technol. 235 (2013) 706.

12. H. Tsuchiya, J. M. Macak, A. Ghicov, L. Taveira, P. Schmuki, Corros. Sci. 47 (2005) 3324.

13. H. C. Choe, Mater. Sci. Forum 654 (2010) 2061.

14. H. C. Choe, Y. H. Jeong, W. A. Brantley, J. Nanosci. Nanotechnol. 10 (2010) 4684.

15. W. G. Kim, H. C. Choe, W. A. Brantley, Thin Solid Films 519 (2011) 4663.

16. J. U. Kim, Y. H. Jeong, H. C. Choe, Thin Solid Films 520 (2011) 793.

17. J. Park, S. Bauer, K. V. D. Mark, P. Schmuki, Nano Lett. 7 (2007) 1686.

18. H. C. Choe, Thin Solid Films 519 (2011) 4652.

19. A. Zhecheva, W. Sha, S. Malinov, A. Long, Surf. Coat. Technol. 200 (2005) 2192.

20. W. Smith, Structure and Properties of Engineering Alloys, 2nd ed., McGraw-Hill, New York, 1993.

21. R. Pederson, Microstructure and Phase Transformation of Ti-6Al-4V, Licentiate Thesis, Lulea University of Technology, 2002.

22. S. Seagle, H. Kessler, in: Principles of Alloying Titanium, 3, ASM Battelle Memorial Institute, Columbus, OH, 1968.

23. T. Nishimura, T. Mizoguchi, Y. Itoh, Kobe Res. Dev. 34 (3) (1984) 63.

24. S. G. Steinemann, surface performance of Titanium, TMS, Warrendale, Pennsylvania, 1996.

25. C. M. Lee, W. F. Ho, C. P. Ju, J. H. C. Lin, J. Mater. Sci.: Mater. Med. 13 (2002) 695.

26. S. L. Assis, I. Costa, Mater. Corros. 58 (2007) 329.

27. B. L. Wang, Y. F. Zheng, L. C. Zhao, Mater. Corros. 60 (2009) 330.

28. X. Liu, P. K. Chu, C. Ding, Mater. Sci. Eng. R 47 (2004) 49.

29. C. A. Grimes, G. K. Mor, TiO_2 nanotube arrays, 2009.

30. Y. T. Sul, C.B. Johansson, Y. Jeong, T. Albrektsson, Med. Eng. Phys. 23 (2001) 329.

31. K. Duan, R. Wang, J. Mater. Chem. 16 (2006) 2309.

32. G. A. Crawford, N. Chawla, Acta Materialia 57 (2009) 854.

33. J. M. Mack, H. Tsuchiya, A. Ghicov, K. Yasuda, R. Hahn, S. Bauer, P. Schmuki, Current Opinion in Solid State and Materials Science 11 (2007) 3.

34. S. H. Kim, Y. H. Jeong, H. C. Choe, J. Nanosci. Nanotechnol. (2013), to be published.

35. H. J. Song, M. K. Kim, G. C. Jung, M. S. Vang, Y. J. Park, Surf. Coat. Technol. 201 (2007) 8738.

36. Y. H. Jeong, H. C. Choe, W. A. Brantley, Appl. Surf. Sci. 258 (2012) 2129.

37. Y. H. Jeong, H. C. Choe, J. Mater. Sci: Mater. Med. 22 (2011) 41.

38. S. H. Jang, H. C. Choe, Y. M. Ko, W. A. Brantley, Thin Solid Films 517 (2009) 5038.

39. P. Jiang, J. Liang, C. Lin, Appl. Surf. Sci. 280 (2013) 373.

40. K. Lee, H. C. Choe, B. H. Kim, Y. M. Ko, Surf. Coat. Technol. 205 (2010)

S267.

41. Y. H. Jeong, H. C. Choe, W. A. Brantley, I. B. Sohn, Surf. Coat. Technol. 217 (2013) 13.

42. J. U. Kim, Y. H. Jeong, H. C. Choe, J. Nanosci. Nanotechnol. 13 (2013) 1876.

감사의 글

논문을 마무리 하면서 이렇게 감사의 글을 쓰고 있는 저의 모습을 보니 2년 반 동안의 치과재료학교실 생활이 떠오릅니다. 그동안의 공부와 많은 새로운 경험들이 쌓이고 쌓여 지금은 소중한 제 인생의 한부분이 되었습니다. 또한 인생의 큰 터닝 포인트였던 시간에 많은 영향을 주신 분과 어려운 과정을 값지게 마칠 수 있도록 도움을 주신 분 들게 짧게나마 감사의 글로 전합니다.

미숙한 점이 많은 제 논문에 많은 관심과 꼼꼼한 지도를 해주시고, 항상 열정적인 가르침과 많은 경험을 가르쳐주기 위해 따뜻한 조언을 아끼지 않으셨던 저의 지도교수님이신 최한철 교수님께 감사드립니다. 또한 바쁘신 가운데도 부족한 제 논문 심사를 흔쾌히 맡아주시고 많은 조언을 베풀어 주셨던 손미경 교수님, 류훈 교수님께도 감사드림을 전하고 싶습니다. 마지막으로 대학원 과정에 도움을 주셨던 치과재료학교실 교수님들이신 김병훈 교수님, 고영무 교수님께도 감사드립니다.

병학형님 항상 도움주시고, 나이차이가 많이 나지만 친구처럼 재미있게 계속 지내요. 은주도 항상 대학생활 처음에 도움 줘서 고마워. 그리고 얼마 얼굴을 못 봤지만 재미있으신 재운형님 항상 연락과 조언을 부탁드리면 도움 주셔서 감사합니다. 나랑 동기이며 가장 친한 친구 중 한명인 현주 항상 이렇게 서로 도움주면서 지내자! 은실이도 어린나이인데 2년 반 동안 실험실 생활 잘 마무리해서 축하해! 채익아! 이제 1년 남았지만 중책을 맡게 되어 부담될 수도 있지만 항상 대학원 생활에 네가 한 부분을 차지하고 있어서 많은 도움이 되었다 고맙다! 이제 대학원 생활을 시작하게 될 인섭이 그리고 김정재 박사님 지금 열심히 하는 모습이 참 보기 좋습니다. 지난 시간이 얼마 안 되어 많은 도움이 되지 못해 미안해. 그리고 졸업하신 선배님들 항상 모이면 조언을 아끼지 않으시고 잘 챙겨주셔서 감사드립니다.

마지막으로 늘 뒤에서 묵묵히 인생의 버팀목이 되어주시고, 제 의견을 항상 존중해 주신 훌륭하신 부모님 항상 감사드립니다. 항상 착하기만 한 내 동생 영환아 또 한 번 취업축하고 항상 이렇게 형제애 있게 지내자!

2014. 02.
성환 올림

저작물 이용 허락서

학 과	광기술공학과 (광응용공학전공)	학 번	20127164	과 정	석사

성 명	한글: 김 성 환 한문 : 金 晟 煥 영문 : Kim Sung-Hwan

주 소	광주광역시 북구 동림동 삼호가든 아파트 102동 505호

연락처	E-MAIL : eyecent86@naver.com

논문제목	한글 : 마이크로 포아와 나노튜브 형성 된 생체용 Ti-25Nb-7Hf 합금의 표면특성 영어 : Surface Characteristics of the Micro-pore and Nanotube Formed Ti-25Nb-7Hf Alloy for Biomaterials

본인이 저작한 위의 저작물에 대하여 다음과 같은 조건아래 조선대학교가 저작물을 이용할 수 있도록 허락하고 동의합니다.

- 다   음 -

1. 저작물의 DB구축 및 인터넷을 포함한 정보통신망에의 공개를 위한 저작물의 복제, 기억장치에의 저장, 전송 등을 허락함
2. 위의 목적을 위하여 필요한 범위 내에서의 편집·형식상의 변경을 허락함. 다만, 저작물의 내용변경은 금지함.
3. 배포·전송된 저작물의 영리적 목적을 위한 복제, 저장, 전송 등은 금지함.
4. 저작물에 대한 이용기간은 5년으로 하고, 기간종료 3개월 이내에 별도의 의사 표시가 없을 경우에는 저작물의 이용기간을 계속 연장함.
5. 해당 저작물의 저작권을 타인에게 양도하거나 또는 출판을 허락을 하였을 경우에는 1개월 이내에 대학에 이를 통보함.
6. 조선대학교는 저작물의 이용허락 이후 해당 저작물로 인하여 발생하는 타인에 의한 권리 침해에 대하여 일체의 법적 책임을 지지 않음
7. 소속대학의 협정기관에 저작물의 제공 및 인터넷 등 정보통신망을 이용한 저작물의 전송·출력을 허락함.

동의여부 : 동의(O)   반대(   )

2014 년 02 월 25 일

저작자: 김 성 환   (서명 또는 인)

조선대학교 총장 귀하